Large-eddy simulation of 3-D corner separation in a linear compressor cascade

Feng Gao, Wei Ma, Gherardo Zambonini, Jérôme Boudet, Xavier Ottavy, Lipeng Lu, Liang Shao

PHYSICS OF FLUIDS **27**, 085105 (2015)

Large-eddy simulation of 3-D corner separation in a linear compressor cascade

Feng Gao,[1,2,a)] Wei Ma,[3] Gherardo Zambonini,[1] Jérôme Boudet,[1,b)]
Xavier Ottavy,[1] Lipeng Lu,[2] and Liang Shao[1]
[1]*Laboratoire de Mécanique des Fluides et d'Acoustique, École Centrale de Lyon, 69134 Écully, France*
[2]*School of Energy and Power Engineering, Beihang University, 100191 Beijing, China*
[3]*School of Aeronautics and Astronautics, Shanghai Jiao Tong University, 200240 Shanghai, China*

(Received 17 February 2015; accepted 28 July 2015; published online 11 August 2015)

The increase of the thrust/weight ratio of aircraft engines is extremely restricted by different 3-D flow loss mechanisms. One of them is the corner separation that can form at the junction between a blade suction side and a hub or shroud. In this paper, in order to further investigate the turbulent characteristics of corner separation, large-eddy simulation (LES) is conducted on a compressor cascade configuration using NACA65 blade profiles (chord based Reynolds number: 3.82×10^5), in comparison with the previous obtained experimental data. Using the shear-improved Smagorinsky model as subgrid-scale model, the LES gives a good description of the mean aerodynamics of the corner separation, especially for the blade surface static pressure coefficient and the total pressure losses. The turbulent dynamics is then analyzed in detail, in consideration of the turbulent structures, the one-point velocity spectra, and the turbulence anisotropy. Within the recirculation region, the energy appears to concentrate around the largest turbulent eddies, with fairly isotropic characteristics. Concerning the dynamics, an aperiodic shedding of hairpin vortices seems to induce an unsteadiness of the separation envelope. © *2015 AIP Publishing LLC*. [http://dx.doi.org/10.1063/1.4928246]

I. INTRODUCTION

Engineers continuously strive to reduce the costs of aircraft propulsion, on both the economic and ecological points of view. A first solution is to increase the efficiency of aircraft engines, particularly in increasing the overall pressure ratio of compressors. A second solution is to decrease the weight of aircraft engines, especially in reducing the number of compressor stages. These result in an increase of the compressor blade loading. However, the compressor blade loading is extremely limited by many 3-D flow losses in compressors, such as boundary layers, flow separations, leakages, and shocks.[1,2]

During the last decades, the impact of corner separation in reducing the blade loading has been emphasized by many researchers, such as Dong *et al.*,[3] Schulz *et al.*,[4] Yocum and O'Brien,[5] Hah and Loellbach,[6] Gbadebo *et al.*,[7] Lei,[8] Choi *et al.*,[9] and Lewin *et al.*[10] A corner separation forms at the junction between an end-wall (hub or casing) and a blade suction surface. It is closed off by limiting streamlines on walls, and a separation vortex is formed on the end-wall near the trailing edge, as sketched in Fig. 1. The main mechanisms of corner separations are:[11] (i) strong adverse pressure gradients, (ii) secondary flows within the passage, (iii) the mixing of the boundary layers on both the end-wall and the blade suction surface, and (iv) a possible horseshoe vortex (when the

a)feng.gao@buaa.edu.cn
b)jerome.boudet@ec-lyon.fr

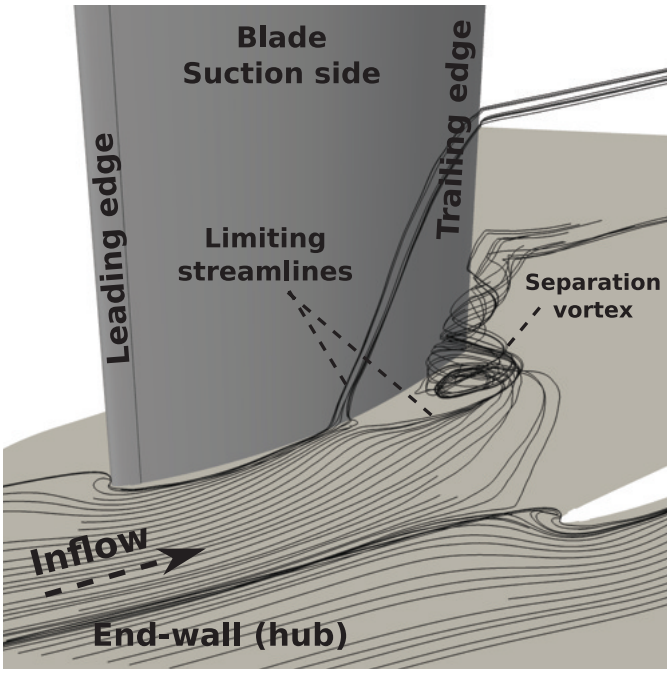

FIG. 1. Topology of corner separation.

blade leading edge is thick).[12] Corner separations are also influenced by many parameters, such as compressor loading,[7] inflow boundary layers,[13] free-stream turbulence intensities,[14] clearance flows,[15] Reynolds number,[16] Mach number,[17] surface roughness,[16] and real blade geometries.[18] As corner separations can reduce the compressor efficiency and can lead to negative consequences, it is requested to control or reduce corner separations.

Some flow control strategies have been investigated on specific blades by researchers.[19–22] But, it is still very difficult to define an effective strategy for controlling corner separations. There are probably two main reasons:

- The mechanisms of corner separations are not yet very clearly understood, particularly the parameters controlling the onset and the size of separations.[7]
- With the rapid development of the computer resources, computational fluid dynamics (CFD) codes based on RANS (Reynolds-averaged Navier-Stokes) equations have integrated turbomachinery design processes. But the conventional RANS turbulence models are very limited in predicting compressor corner separations. Therefore, the control strategies which are developed using these turbulence models are not always reliable.[23–25]

In order to realize a control strategy, it is required to settle these two problems above.

A series of experimental work has been previously conducted by some of the current authors.[26] Accurate and detailed measurements have been achieved by a hot-wire anemometry, static pressure tubes, a five-hole probe, a Laser-Doppler anemometry (LDA), and a Particle Image Velocimetry (PIV). A bimodal phenomenon is for the first time, as believed by the authors, measured in an internal flow corner separation configuration without leakages. Furthermore, with the experimental data, the authors also studied the outer peak appeared on the profile of streamwise Reynolds stress and inferred that the adverse pressure gradient is not a trigger for the appearance of the outer peak but can accelerate it.[27] Insights have been brought by the experiment, but they are still limited by the measurement technologies to illustrate structures of the corner separation as well as the turbulent characteristics within the corner separation region.

Validated numerical results are then desired to interpret the singular phenomenon observed in the experiment, in combination with the experimental data. Also, they are needed to provide more insights into the mechanisms where experimental technologies are limited.

RANS solves the Reynolds-averaged Navier-Stokes equations and demands moderate computational resources. But the results are highly dependent on the choice of the turbulence modeling. Some conventional RANS models, such as the Spalart-Allmaras (SA) model and the standard Wilcox $k-\omega$, are found to over predict the corner separation.[23,25] These models were constructed and validated in simple boundary layer flows, so they often fail to reproduce flow fields under complex geometries with reversed flows. Large-eddy simulation (LES), an alternative between the direct numerical simulation (DNS) and RANS, permits the reduction of costs (compared to DNS) and investigations of turbulent flow characteristics. Just as the name implies, the large-scale turbulent eddies are directly solved, while the small-scale ones are modeled by subgrid-scale (SGS) models. Fortunately, with the rapid development of computer technologies, it becomes possible to use LES to investigate the flow mechanisms of complex geometries.[28–30] In addition, LES has proven to be capable to predict turbomachinery flows.[31]

Therefore, the main content of the paper is to conduct a LES to simulate the corner separation found in the previous experimental work[26] (Section III), and then to validate it with the experimental data (Section IV). Finally, the validated LES results are used to analyse the turbulent dynamics within the corner separation region (Section V).

II. CONFIGURATION AND AVAILABLE EXPERIMENTAL RESULTS

Before getting into the numerical validation and analysis, let us recall the experimental configuration and the measurements previously conducted by Ma *et al.*[26]

The test rig used in the experimental investigation is a linear compressor cascade consisting of 13 modified NACA65 blade profiles, as shown in Fig. 2, with the parameters listed in Table I. The free-stream velocity in the wind tunnel is set to $U_\infty = 40.0$ m/s to yield a blade-chord based Reynolds number $Re_c = 3.82 \times 10^5$. The turbulence intensity is about 0.8% in the free-stream. The focus is put on the incidence angle of 4° in this paper, since in this configuration, a significant corner separation is observed. In order to investigate the corner separation as encountered in compressors without the impact of laminar-turbulent transition processes and to reduce difficulties for numerical simulations, tripping bands (3.0 mm wide by 0.3 mm thick, located at 6.0 mm from the leading edge) are used in the experiment on both the pressure and suction sides,[32] as suggested by Evans.[33] Since the classic RANS models consider the flow to be fully turbulent, the tripping bands also allow the RANS simulations to simulate the mean flow without transition problems. The available experimental results are listed in Ref. 26.

III. NUMERICAL METHODS

In this paper, a LES is carried out in order to investigate the turbulent characteristics of the corner separation. The simulation is performed using an in-house finite-volume compressible N-S equation solver *Turb'Flow*[31,34] developed in LMFA (at *École Centrale de Lyon*).

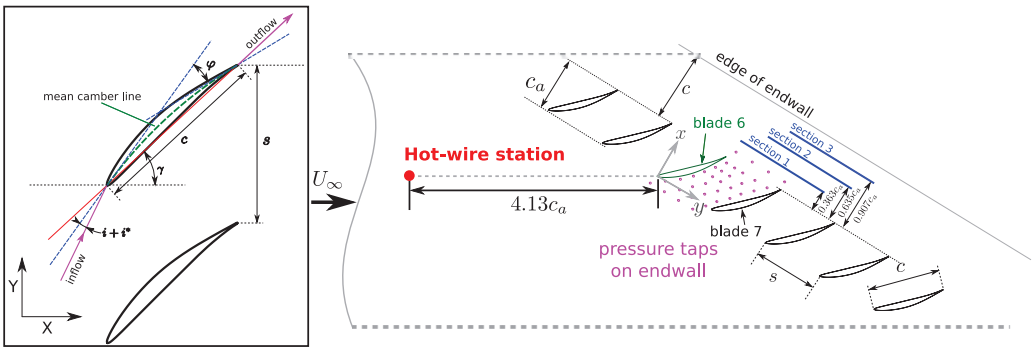

FIG. 2. Sketch of the compressor cascade configuration.

TABLE I. Parameters of the cascade.

Name	Symbol	Magnitude
Chord	c	150.0 mm
Camber angle	φ	23.22°
Stagger angle	γ	42.7°
Pitch	s	134.0 mm
Blade span	h	370.0 mm
Incidence angle	i	4°
Free stream velocity	U_∞	40.0 m/s
Chord-based Reynolds number	Re_c	3.82×10^5

The shear-improved Smagorinsky model (SISM) model of Lévêque *et al.*[35] is used to estimate the SGS eddy viscosity. This model has been devised from the analysis of the scale-by-scale energy budget of locally homogeneous shear turbulence. It is thus grounded on physical considerations. Furthermore, its formulation is simple and its computational cost is moderate. It has been applied to complex flows, such as a cylinder flow[36] or the tip-flow of a fan.[31]

The SISM model is inspired by the original Smagorinsky model, with an additional term related to the mean shear magnitude $|\langle\widetilde{S}\rangle|$, as given in Eq. (1),

$$\mu_{sgs} = \overline{\rho}(C_s\Delta)^2(|\widetilde{S}| - |\langle\widetilde{S}\rangle|), \tag{1}$$

with $C_s = 0.18$ denoting the standard Smagorinsky constant and Δ representing the grid spacing (computed as the cube root of the grid cell volume). The magnitude of the resolved strain rate $|\widetilde{S}|$ is computed as $(2\Sigma_{i,j}\widetilde{S_{ij}}\widetilde{S_{ij}})^{1/2}$. It is important to note that the model uses the difference of the magnitudes of strain (resolved and mean), and not the magnitude of the difference. The angular brackets $\langle\ \rangle$ *a priori* denote an ensemble average, but is practically represented by an exponential smoothing in the present work, following the work of Cahuzac *et al.*[36]

Under this conception, the SGS eddy viscosity can encompass two kinds of interactions:[35,36] (i) interactions between the mean velocity gradient and the resolved fluctuating velocities (the rapid part of the SGS fluctuations[37]) and (ii) interactions between the resolved fluctuating velocities themselves (the slow part of the SGS fluctuations). The rapid part is associated with the large-scale eddy distortion, and the slow part corresponds to the Kolmogorov energy cascade.

A. Numerical schemes

A 4-point centered spatial scheme (Jameson *et al.*[38]) is used for the inviscid fluxes discretization, with a fourth-order artificial viscosity (viscosity coefficient:[39] 0.002). This enables to damp spurious grid-to-grid oscillations, with a moderate level of numerical dissipation. The viscous fluxes are interpolated by a 2-point centered scheme.

A three-step Runge-Kutta scheme with a global constant time step 2.5×10^{-8} s is employed for the temporal discretization. In consideration of the minimum grid size 1×10^{-5} m, the reference velocity 40 m/s and the sound speed 340 m/s, a Courant number (Courant-Friedrichs-Lewy condition) close to 0.95 is achieved.

More details about the numerical schemes, and evaluations on a flat-plate boundary layer case, can be found in Ref. 39.

B. Grid and boundary conditions

The blade-to-blade mesh is drawn in Fig. 3 for every fourth point. Only one blade passage is simulated. The sand-papers used in the experiment are considered in the LES by removing some grid points at the same locations. This mesh is duplicated along the spanwise direction into 481 planes (half span) to obtain a 3-D mesh. The sizes of the grid at the wall, in wall units, are $\Delta x^+ \le 60$, $\Delta y^+ \le 1$, and $\Delta z^+ \le 30$, in the streamwise, wall-normal, and cross-stream directions, respectively,

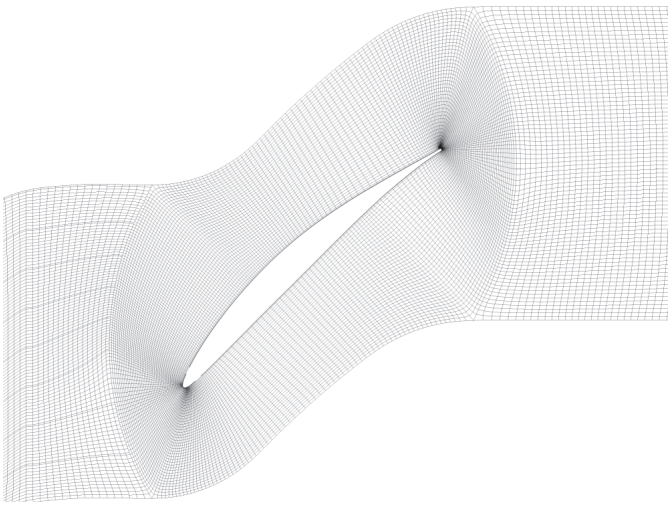

FIG. 3. View of the LES mesh around the blade. Every fourth point is shown.

on both the blade surface and the end-wall. Therefore, the total number of grid points in the blade passage is about 200×10^6. The inlet plane is located at the same location as the hotwire measurement station (the hotwire station can be seen in Fig. 2). The inflow conditions are imposed using a 3-D boundary layer simulation that has been configured to fit the experimental boundary layer (see Section III C for details). The outlet plane is located one chord (in the axial direction) downstream of the experimental outlet, aiming to damp the numerical reflections. For the same purpose, the mesh is stretched near the outlet plane and an explicit filter[40] is also used (details are discussed in Section III D). Since only one half of the blade span is simulated to reduce the computational cost, the mid-span is set to be symmetric and the pitchwise boundaries are connected by a periodic condition. Both the blade surface and the end-wall are set to be non-slip adiabatic walls. The explicit filter is also used over five grid planes near the blade leading edge and the trailing edge to ensure the computational stability (discussion can be found in Section III D).

C. Inflow condition

In order to provide turbulent conditions on the inlet plane of the linear compressor cascade, a 3-D boundary layer simulation on a flat plate is performed in parallel with the blade passage simulation. At the location where the time-averaged displacement thickness δ_1 meets the experimental one (measured by the hot-wire), the fluctuating information is transferred to the compressor cascade inlet at every time step. Moreover, the same shape factor H_{12} is found in the experiment and the LES; therefore, the momentum thickness δ_2 is automatically matched.

As regards LES, only the incidence angle 4° is simulated. The computational domain of the inlet boundary layer is about 2.54 m long, while the width in the cross-flow direction and the height in the direction perpendicular to the flat plate wall are set to be greater than δ_{99} and $2\delta_{99}$, respectively. The grid size at the wall is similar to the cascade simulation ($\Delta x^+ \leq 60$, $\Delta y^+ \leq 1$, and $\Delta z^+ \leq 30$) and the number of points for the incoming boundary layer is about 100×10^6.

The transition of the boundary layer simulation is triggered at the streamwise location $Re_x = 3 \times 10^5$ by a tripping band of 4.8×10^{-3} m long by 6.73×10^{-4} m thick. The band is modeled by removing cells from the smooth mesh, and the dimensions are chosen following the work of Boudet *et al*.[39] However, the thickness of the tripping band is set to be twice the design value in order to achieve the displacement thickness target.

Four quantities, density and the three components of velocity, are transferred from the selected section in the flat plate simulation to the inlet plane of the linear compressor cascade, in order to impose a turbulent boundary layer on the end-wall, as depicted in Fig. 4. Within the boundary layer region, these four quantities on the selected source plane (filled by "/" lines in the figure) are sent with space periodicity to the linear compressor cascade inlet plane (also filled by "/" lines). Out of

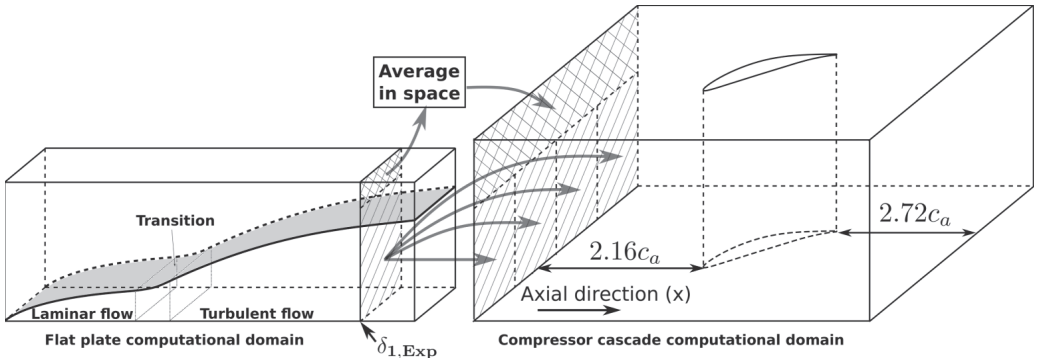

FIG. 4. Sketch of the inflow condition.

the boundary layer, the turbulent intensity is very small in both the experiment and the simulation. Therefore, the free-stream values on the selected source plane (filled by "X" lines) are spatially averaged, then homogeneously imposed on the upper region of the linear compressor cascade inlet plane (also filled by "X" lines). Note that this approach applies at each time step.

Some parameters of the inflow boundary layer at the cascade inlet plane are listed in Table II. A good agreement is achieved between the LES and the experiment, with however a 7.6% underestimate of the friction velocity u_τ by the LES. Non-dimensional mean velocity profiles are plotted in Fig. 5. The experimental and LES results are compared with the DNS results of Sillero *et al.*[41] at $Re_{\delta_2} = 6500$. The experimental results agree with the DNS. Some discrepancies are seen in the LES results for the region outside the viscous layer, due to the underestimate of the friction velocity u_τ.

A comparison of the flow conditions with other linear and annular compressor cascades is summarized in Table III. The Reynolds number and relative boundary layer thickness are comparable to those encountered in other compressor cascades, which implies that the flow condition of the present corner separation configuration is relevant.

D. Explicit filter

Since numerical acoustic reflections are often encountered in unsteady simulations using compressible Navier-Stokes equation solvers, attention should be paid to the outlet condition. The explicit filter introduced by Bogey and Bailly[40] is implemented over the last 20 grid planes upstream of the outlet, aiming at damping the numerical reflections. The five conservative variables $\rho, \rho u, \rho v, \rho w, \rho e_t$ are filtered. The filter is expressed as follows:

$$\eta(i) = \frac{i - i_{begin} + 1}{i_{end} - i_{begin} + 1}, (i_{begin} \le i \le i_{end}), \tag{2}$$

$$\sigma(\eta) = \alpha \cdot \eta^\beta, \tag{3}$$

where the magnitude of the filtering is controlled by the amplitude α $(0 \le \alpha \le 0.45)$ and the exponent β $(1 \le \beta \le 2)$. For a given variable q, the filtered value $\overline{q}$ expresses as

$$\begin{aligned} \overline{q}_{i,j,k} &= q_{i,j,k} - \sigma[q_{i,j,k} - (q_{i-1,j,k} + q_{i+1,j,k} + q_{i,j-1,k} + q_{i,j+1,k} + q_{i,j,k-1} + q_{i,j,k+1})/6] \\ &= (1-\alpha)q_{i,j,k} + \frac{\alpha}{6}(q_{i-1,j,k} + q_{i+1,j,k} + q_{i,j-1,k} + q_{i,j+1,k} + q_{i,j,k-1} + q_{i,j,k+1}), \end{aligned} \tag{4}$$

where i, j, and k are the grid indices, with "i" along the axial direction.

TABLE II. Parameters of the inflow boundary layer, at the cascade inlet.

	δ_{99} (mm)	δ_1 (mm)	δ_2 (mm)	$H_{12} = \delta_1/\delta_2$	u_τ (m/s)	$Re_{\delta_2} = U_\infty \delta_2/\nu$
Experiment	30.0	3.7	2.8	1.32	1.45	7200
LES	27.3	3.7	2.8	1.31	1.34	7400

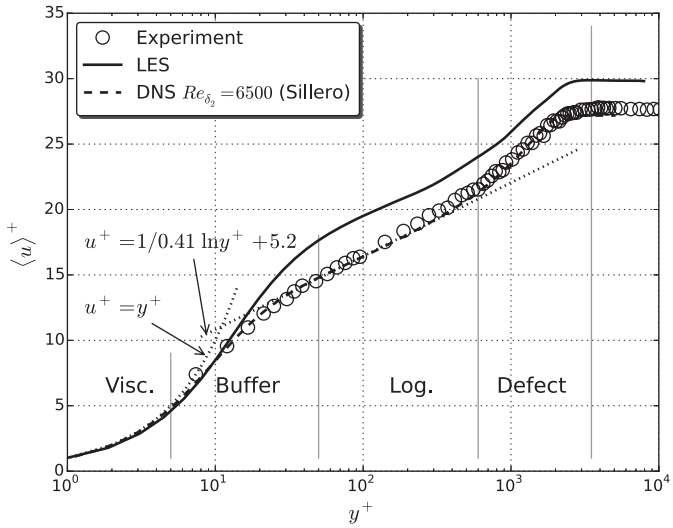

FIG. 5. Normalized mean velocity profiles at the cascade inlet.

In this paper, α and β are set as 0.05 and 2.0, according to the experience of Ye.[44]

It can be seen, through the filter's equation, that the filter can be considered as a smoother in practice. The conservative quantities are smoothed close to the outlet. Inspired by this, the authors also put the filter near the blade leading and trailing edges over five grid points, so that the oscillations can be smoothed. To be sure that the flow field is not disturbed by the implementation of the explicit filter, a test has been previously conducted on a flat plate simulation: an explicit filter was installed in the turbulent boundary layer over 5 grid points near the wall, and the statistic quantities downstream were found identical to the case without the filter.

E. Evaluation of the simulation's quality

In total, 2×10^6 CPU hours, on 856 Xeon E5450 4C processor cores, has been consumed for the convergence of the computation and the analysis. About nine periods of advection of the fluid through the inter-blade channel (c/U_∞) have been used for the analysis.

In LES, the SGS tensor appears after filtering the Navier-Stokes equations, and it is modeled by the SGS model. The main idea is generally to add some extra viscosity to simulate the diffusion and dissipation processes. Geurts and Frölich[45] proposed a subgrid-activity parameter to characterize the share of the modeled dissipation,

$$s = \frac{\langle \varepsilon_{sgs} \rangle}{\langle \varepsilon_{sgs} \rangle + \langle \varepsilon_\mu \rangle}, \tag{5}$$

where $\langle \varepsilon_{sgs} \rangle$ is the SGS dissipation, and $\langle \varepsilon_\mu \rangle$ is the viscous turbulence dissipation. According to the definition, $0 \leqslant s < 1$, with $s = 0$ corresponding to DNS and $s = 1$ to LES at an infinite Reynolds number.

The subgrid-activity parameter is computed using the LES results for both the regions at mid-span and close to the end-wall, as shown in Fig. 6. The values of the subgrid-activity parameter

TABLE III. Comparison of the flow conditions with other compressor cascades.

Cascade	Re_c	Measurement position	$\delta_1/c \times 1000$	$\delta_2/c \times 1000$
Current, linear	3.82×10^5	$x = -2.16c_a$	24.7	18.7
Bario *et al.*,[42] linear	7.5×10^5	$x = -0.60c_a$	26.6	14.9
Dong *et al.*,[3] annular	3.0×10^5	Shown in Fig. 1 of Ref. 3	28.0	18.0
Beselt *et al.*,[43] annular	3.0×10^5	$x = -0.032c_a$	25.9 ~ 47.1	18.5 ~ 33.6

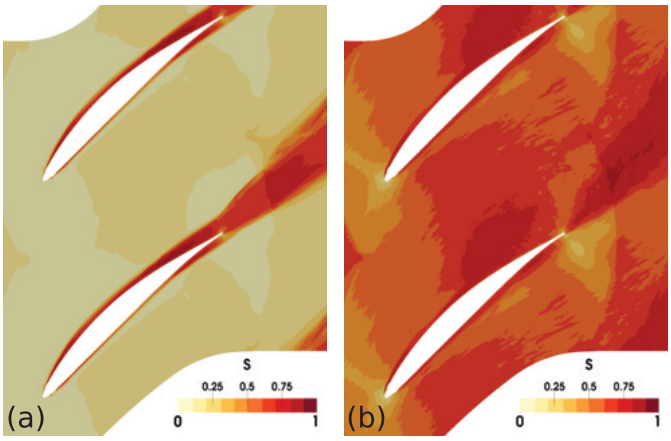

FIG. 6. Subgrid-activity parameter. (a) At mid-span and (b) close to the end-wall.

are always greater than 0, implying that the subgrid-scale model is active in this LES. Meanwhile, the fact that s is less than 0.85 for the whole computation domain shows a good resolution of the mesh, and it also implies that the subgrid-activity is appropriate. At mid-span (refer Fig. 6(a)), the subgrid-activity parameter is very small for most of the regions. High values are observed close to the blade and in the wake region, suggesting that the SGS model is more active in these zones. Close to the end-wall, as shown in Fig. 6(b), the values of the subgrid-activity parameter are more significant, which means that the SGS model plays a more important role close to the end-wall than at mid-span. The highest values of the subgrid-activity parameter are found in the corner separation region and the wake region. These regions of more intense turbulent activity necessitate a stronger SGS dissipation.

IV. RESULTS

In this section, the LES results are going to be validated with the experimental results.

A. Classification of corner separation

The authors would like to classify the corner separation using Lei's criterion,[46] which is very popular.

The diffusion parameter D is calculated from the geometric parameters, while the stall indicator S is computed from the experimental/LES results, and they are shown in Fig. 7. Interestingly, the D parameter drops in the small corner separation area, but both the experimental and LES stall indicators join the upper branch, indicating a massive corner separation ("corner stall" according to Lei *et al.*). The experiment and the LES are in fairly good agreement, and they both controvert Lei's criterion. This criterion was constructed based on RANS simulations over about 100 different cascade geometries, and then validated with the available data in the literature. The criterion was found in agreement with all the rotor data provided, but was not directly compared with stator data. This criterion is very useful in turbomachinery design processes as it is easy to compute with cascade geometric parameters, but the present results suggest it should be re-evaluated.

B. Static pressure coefficient on the blade

The blade surface static pressure coefficient $C_p = (P_s - P_{s,\infty})/(P_{t,\infty} - P_{s,\infty})$ is an important parameter in this investigation, since the operating conditions of the compressor cascade are easily monitored by it (P_s: static pressure, P_t: total pressure, and ∞ subscript: inflow conditions). P_s is measured by static pressure tubes embedded in the blade. The mean C_p distributions around the blade from the mid-span to the end-wall are shown in Fig. 8. The circles with vertical error bars

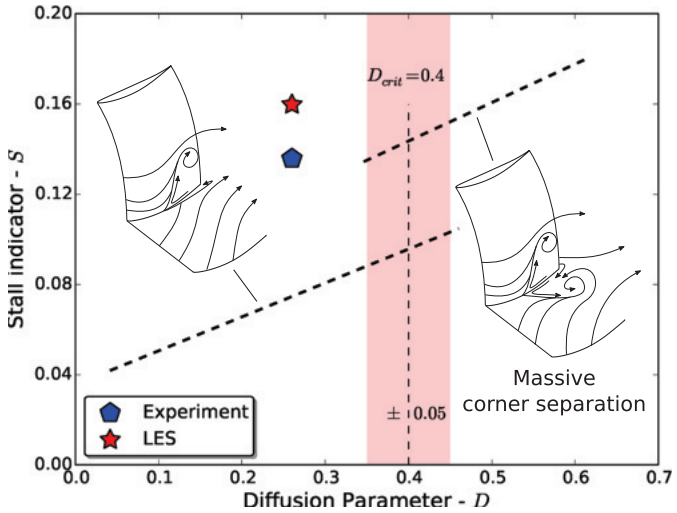

FIG. 7. Classification of the corner separation by Lei's criterion.

denote the experimental results and the corresponding uncertainties, while the solid lines are LES results. The upper branch indicates the static pressure coefficient on the pressure side, and the bottom branch represents the C_p on the suction side. Some oscillations appear in the numerical results near the blade leading edge, due to the implementation of the tripping bands.

At mid-span, a good agreement is observed between the experimental and LES results, as shown in Fig. 8(a). On the suction side, C_p decreases rapidly and then increases regularly until the trailing edge. This corresponds to the evolution of the velocity outside the boundary layer: the fluid at first accelerates and then decelerates until the trailing edge. On the pressure side, downstream of the fluid acceleration region (the acceleration region begins near the leading edge and ends at about $x/c_a = 0.15$), the pressure is nearly uniform. Towards the end-wall (from Figs. 8(a)–8(d)), the area enclosed by the C_p lines gets smaller, indicating a decrease of the blade loading. It can be seen that

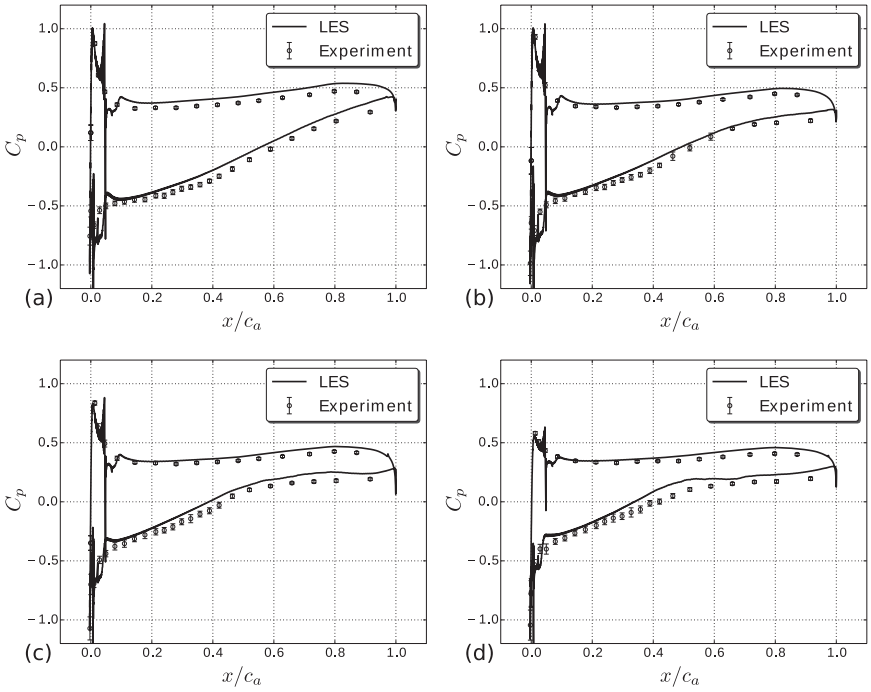

FIG. 8. Mean static pressure coefficient. (a) At mid-span ($z/h = 50.0\%$), (b) $z/h = 16.2\%$, (c) $z/h = 5.4\%$, and (d) close to the end-wall ($z/h = 1.4\%$).

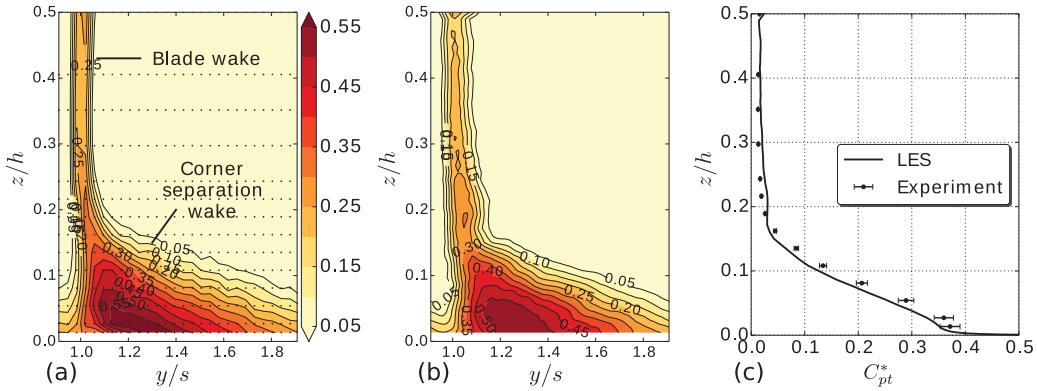

FIG. 9. Mean total pressure loss coefficient at the outlet section 1. (a) Experiment C_{pt}, (b) LES C_{pt}, and (c) pitchwise-mass-averaged total pressure loss coefficient C_{pt}^*.

the LES results follow fairly well the experimental ones from the mid-span to the end-wall. At the spanwise location $z/h = 5.4\%$ in Fig. 8(c), a plateau (constant static pressure region) appears on the aft part of the blade suction side, due to the corner separation. The beginning of the plateau indicates the onset of the corner separation at the current spanwise location. Very close to the end-wall, in Fig. 8(d), the onset of the plateau (and thus the separation) occurs earlier, further reducing the area enclosed by the C_p lines. Therefore, the blade loading is reduced close to the end-wall by the development of the corner separation.

C. Total pressure losses

Total pressure losses are a key indicator to evaluate the performance of compressors. The expression of the total pressure loss coefficient is given by $C_{pt} = \frac{P_{t,\infty} - P_t}{P_{t,\infty} - P_{s,\infty}}$, where P_t denotes the local total pressure. It is plotted at the outlet section 1, 0.363 axial chord length downstream of the blade trailing edge, in Fig. 9. The dots denote the measurement points in Fig. 9(a) for the experimental results by the 5-hole probe. The wakes of the blade and the corner separation are clearly observed, through the higher values of C_{pt}.

According to the contours, a good agreement is achieved between the experimental and LES results. The simulation captures both the extent and the intensity of the losses induced by the corner separation.

In order to get a more direct impression about the losses, the C_{pt} is mass-averaged in the pitchwise direction, yielding a pitchwise-mass-averaged total pressure loss coefficient C_{pt}^*, expressed in Eq. (6),

$$C_{pt}^* = \frac{\int_0^s C_{pt}(y,z)\rho(y,z)u(y,z)dy}{\int_0^s \rho(y,z)u(y,z)dy}, \tag{6}$$

where the density $\rho(y,z)$ is considered to be constant, as the flow is incompressible in this study. This coefficient is plotted in Fig. 9(c). The LES results match the experimental ones. The pitchwise-mass-averaged losses induced by the trailing edge wake are fairly well simulated by LES. The corner separation losses extend to about $z/h = 0.17$ according to both the experimental and LES results. Furthermore, the LES accurately predicts the intensity of the losses induced by the corner separation. This demonstrates the capability of the LES to correctly simulate the losses induced by the separation itself, but also by the mixing process downstream of the separation.

D. Mean and fluctuating velocity profiles along the blade suction surface

The LES results have been well validated in terms of turbomachinery parameters: the static pressure coefficient around the blade and the total pressure losses. In order to analyze the turbulent

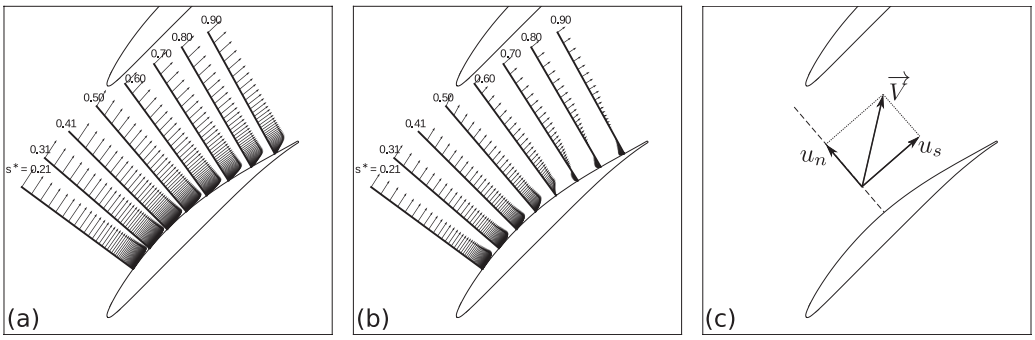

FIG. 10. Time-averaged velocity vectors along the blade suction surface. (a) At mid-span ($z/h = 48.6\%$), (b) near the end-wall ($z/h = 1.4\%$), and (c) velocity decomposition.

characteristics within the corner separation region, the results' reliability also needs to be checked from the point of view of turbulence, through the mean and fluctuating velocity profiles.

1. At mid-span

At mid-span, although the quasi 2-D flow in this region appears to be less complex than that in the 3-D unsteady corner separation region, it encounters high adverse pressure gradients and curved geometry effects.

The mean velocity vectors are plotted in Fig. 10(a). Eight stations are extracted along and perpendicularly to the blade suction surface. According to the 2-D velocity vectors, no separation is found at mid-span. A more detailed comparison is realized by decomposing the velocity into a tangential direction s (parallel to the blade surface) and a wall-normal direction n (perpendicular to the blade surface), see Fig. 10(c).

Figure 11(a) shows the evolution of the tangential velocity profiles on the blade suction surface at mid-span for each measurement station. They are plotted in semi-log scale. The black lines are the LES results, the blue "x" denote the available PIV results at the last three measurement stations, and the red symbols with the horizontal and vertical bars represent the LDA results and their corresponding uncertainties (horizontal and vertical bars for measurement and location uncertainties, respectively). An excellent agreement is observed between the LES, PIV, and LDA results. From the leading edge to the trailing edge, the boundary layer thickens gradually. Meanwhile, the free-stream velocity decreases. Near the leading edge, the near-wall peak of the tangential velocity corresponds to the near-wall flow acceleration. This peak is reduced when flowing towards the trailing edge, indicating the deceleration of the near-wall fluid. Close to the trailing edge, the near-wall tangential velocity gradient in the wall-normal direction decreases significantly, and so does the wall shear stress, implying that the boundary layer is about to separate.

The velocity fluctuations refer to the root mean square of the Reynolds normal stresses. The tangential velocity fluctuations at mid-span are plotted in Fig. 11(b), in semi-log scale. A good agreement is observed in the free-stream between the LES, PIV, and LDA results, with very low values. Close to the blade wall, the LES has captured the classic peak region of $u'_{s,rms}/U_\infty$ appeared in the experiment, on the first four measurement stations. Some discrepancies appear on the last four measurement stations. From the first measurement station $s^* = 0.21$ to the last measurement station $s^* = 0.90$, the peak location moves progressively away from the wall. On the measurement station $s^* = 0.70$, a flat region appears around the peak of the velocity fluctuations. With the development of the boundary layer towards the trailing edge, the $u'_{s,rms}/U_\infty$ profile seems to show up two peaks. This two-peak shape is also observed by other researchers in boundary layer flows under adverse pressure gradients.[27,47]

2. Close to the end-wall

Near the end-wall, additional effects influence the suction-side boundary layer, beside the streamwise and pitchwise pressure gradients. Secondary flow structures can develop within the

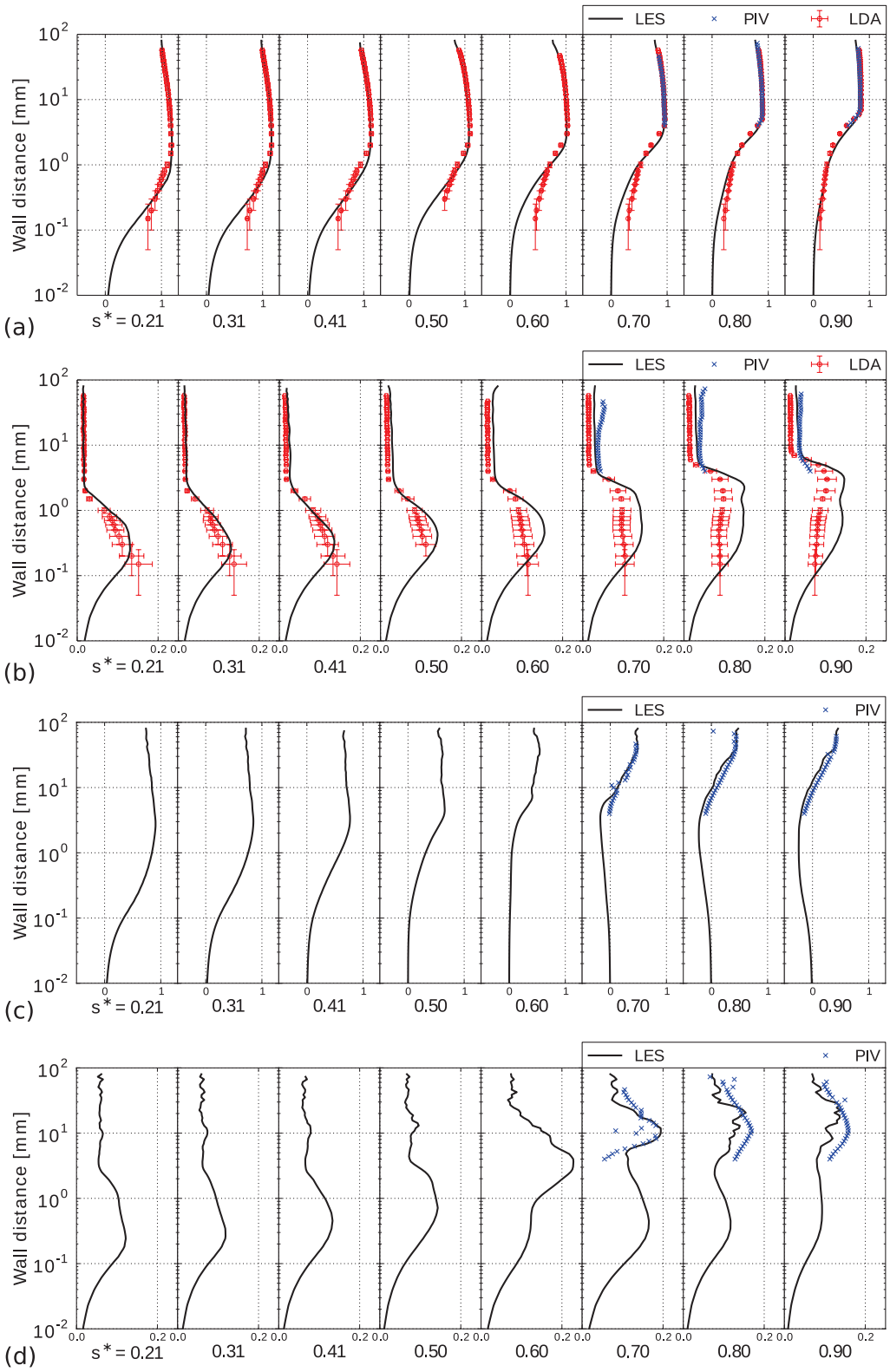

FIG. 11. Tangential velocity profiles (mean and RMS fluctuations) on the suction side. (a) and (c): Time-averaged tangential velocity profiles $\langle u_s \rangle / U_\infty$; (b) and (d): tangential velocity fluctuations (RMS) $u'_{s,rms}/U_\infty$. (a) and (b): At mid-span ($z/h = 48.6\%$); (c) and (d): close to the end-wall ($z/h = 1.4\%$). Black lines: The LES results; blue "x:" the available PIV results; red symbols: the LDA results and the corresponding uncertainties (horizontal and vertical bars for measurement and location uncertainties, respectively).

inter-blade channel (e.g., passage vortices[2]). There is also an influence of the thick end-plate boundary layer, which reduces the mean flow velocity and increases the turbulent intensity. These effects lead to three-dimensional corner separation.

The mean velocity vectors on the measurement stations are shown in Fig. 10(b) and the mean tangential velocity profiles are compared in Fig. 11(c). The fluid acceleration near the blade leading edge is observed through the near-wall peak of the tangential velocity component $\langle u_s \rangle / U_\infty$ from $s^* = 0.21$ to 0.50. The boundary layer thickens gradually from the first measurement station $s^* = 0.21$ towards the trailing edge, and the velocity gradient associated with the wall friction becomes smaller and smaller. The flow separates around the measurement station $s^* = 0.60$, since the velocity gradient close to the blade wall is nearly zero. Then, the near-wall velocity gradient becomes negative at $s^* = 0.70$, which means that the flow is separated, and the reversed flow region expands downstream. The most intense reversed flow is observed on the measurement stations $s^* = 0.80$ and $s^* = 0.90$. This indicates that the "corner separation center" (the focus of the recirculation region) is located close to these two measurement stations. A very good agreement is achieved on the tangential velocity profiles between the LES and PIV results on the last three measurement stations.

The evolution of the RMS of the tangential velocity fluctuations $u'_{s,rms}/U_\infty$ is plotted in Fig. 11(d). From the measurement station $s^* = 0.21$ to $s^* = 0.41$, a single peak of $u'_{s,rms}/U_\infty$ is observed, and both the value and the wall distance of the peak grow, as observed for the fluctuations at mid-span. On the measurement station $s^* = 0.50$, a flat region seems to appear around 1 mm from the wall. This flat region forms much earlier than that close to the mid-span, which appears at $s^* = 0.70$ (see Fig. 11(b)). At $s^* = 0.60$, where the flow tends to separate, two peaks of $u'_{s,rms}/U_\infty$ appear. Downstream, the outer peak decreases but still dominates the inner one. Moreover, the wall distance of the outer peak increases in the separation. On the last three measurement stations, a good agreement is observed between the LES and the PIV around the outer peak. The outer peak is well developed in the corner separation region. It should be noted that from the measurement station $s^* = 0.60$ to $s^* = 0.90$, the outer peak is located much closer to the end-wall than to the blade, which means that the end-wall boundary layer may have more impact on the outer peak than the suction side boundary layer.

V. TURBULENT DYNAMICS

In Sec. IV, the LES results have been very well validated with the experimental data, in terms of turbomachinery performance parameters (static pressure and total pressure losses) and also turbulent boundary layer profiles (mean velocity profiles and fluctuating velocity profiles) both at midspan and close to the endwall. That brings confidence, in using the LES results, to further investigate and to provide more insights into the turbulent dynamics of the corner separation.

In this section, the authors attempt to discuss the turbulent dynamics of the corner separation, in terms of unsteady turbulent structures, one-point velocity spectra, and turbulent anisotropy characteristics.

A. Unsteady turbulent structures

Experiments can capture unsteady flow features within certain areas, but cannot reproduce the whole process of the corner separation vortices formation and breaking down, especially because the uncertainties of the experimental results are significant close to the walls. RANS results can provide an entire flow field, but cannot describe turbulent eddies. The validated LES results therefore are a very good database to illustrate the unsteady turbulent structures of the corner separation, with their formation and breaking down processes.

The well-known vortex identification criterion Q, corresponding to the second invariant of the velocity gradient tensor,[48] is utilized here to illustrate the turbulent coherent structures of the corner separation. The Q-criterion is expressed by the following equation:

$$Q = \frac{1}{2}(\Omega_{ij}\Omega_{ij} - S_{ij}S_{ij}), \tag{7}$$

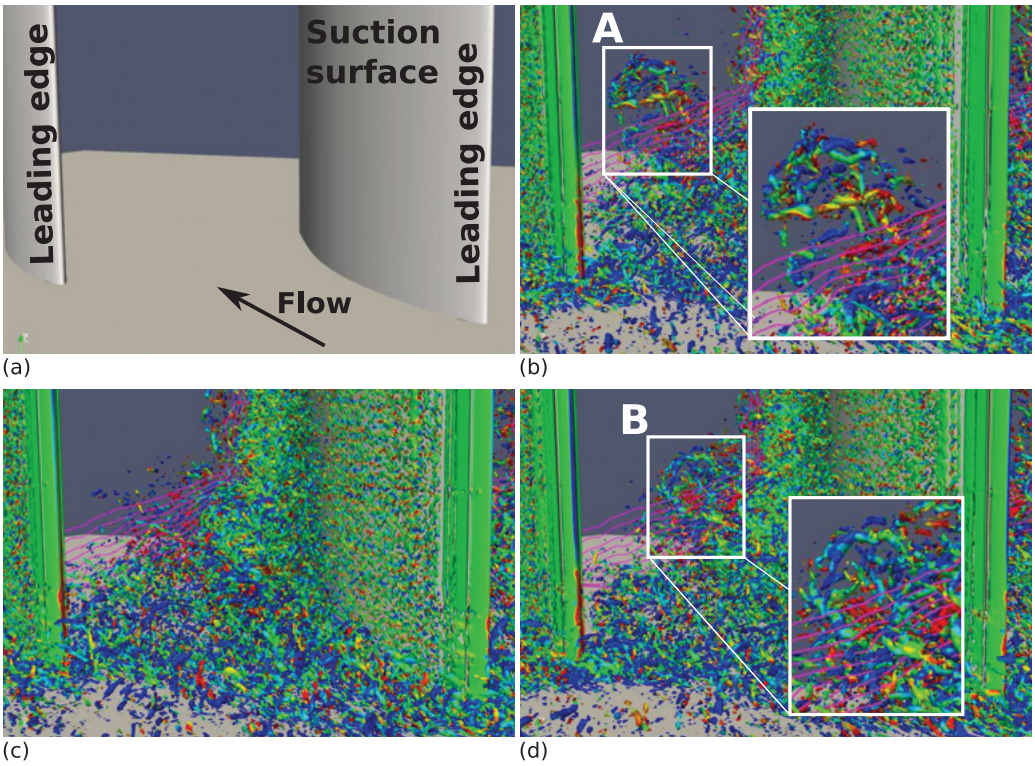

FIG. 12. Turbulent structures shown by iso-surfaces of Q criterion ($Q = 120U_\infty^2/c^2$), and colored by the axial vorticity. Every two point is used to calculate the value of Q. (a) Schematic, (b) $t = 0.00c/U_\infty$, (c) $t = 2.40c/U_\infty$, and (d) $t = 4.27c/U_\infty$.

where Ω_{ij} and S_{ij} are the anti-symmetric and the symmetric components of the velocity gradient tensor (i.e., the rate-of-rotation tensor and the rate-of-strain tensor), respectively. Their expressions are given below as

$$\Omega_{ij} = \frac{1}{2}\left(\frac{\partial u_i}{\partial x_j} - \frac{\partial u_j}{\partial x_i}\right), \tag{8}$$

$$S_{ij} = \frac{1}{2}\left(\frac{\partial u_i}{\partial x_j} + \frac{\partial u_j}{\partial x_i}\right). \tag{9}$$

The Q-criterion represents the local equilibrium between the rotation rate and the strain rate. A positive value of Q indicates a region where the rotation exceeds the strain.[49]

A schematic of the compressor cascade with the flow direction is illustrated in Fig. 12(a). The evolution of the turbulent structures in the corner separation region is shown in Figs. 12(b)–12(d) through iso-surfaces of Q-criterion, with $Q = 120U_\infty^2/c^2$. The iso-lines of the total pressure loss coefficient, which is shown in Fig. 9(b), are also drawn in these figures. Three instants of the flow are presented. At the time 0, a large-scale hairpin vortex (A) is clearly observed downstream of the corner separation region, as shown in Fig. 12(b). At the time $2.40c/U_\infty$, in Fig. 12(c), the vortex (A) has broken down and is no longer observed. Later, at the time $4.27c/U_\infty$, another large-scale hairpin vortex (B) appears. The vortex is created in the separated region at some instants, and subsequently expelled.

The streamlines close to the wall ($z/h = 1.4\%$) at the same instants are illustrated in Fig. 13. From $t = 0.00c/U_\infty$ to $t = 2.40c/U_\infty$, the recirculation region becomes larger. Then, at $t = 4.27c/U_\infty$, the recirculation region returns to a small one.

It is then interesting to consider together the Q criterion and the streamlines. At the first instant ($t = 0.00c/U_\infty$, Figs. 12(b) and 13(a)), where a small recirculation region is seen from the streamlines, there is a large-scale vortex (A) downstream of the corner separation region. At the second instant ($t = 2.40c/U_\infty$), a large recirculation region is observed in Fig. 13(b), but no vortex can be

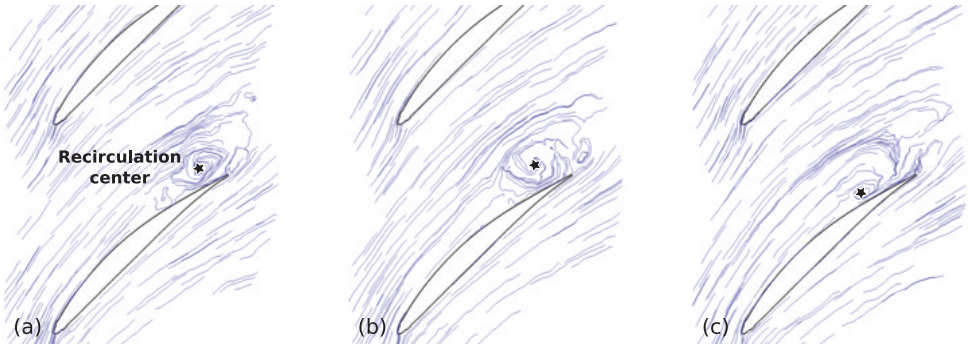

FIG. 13. 2-D instantaneous streamlines close to the end-wall ($z/h = 1.4\%$). (a) $t = 0.00c/U_\infty$, (b) $t = 2.40c/U_\infty$, and (c) $t = 4.27c/U_\infty$.

seen in Fig. 12(c). At the last instant ($t = 4.27c/U_\infty$, Figs. 12(d) and 13(c)), the recirculation returns to a small one, and a large-scale vortex (B) is seen again downstream of the corner separation region. This seems to indicate a vortex shedding process, where the release of the hairpin vortex induces a contraction of the recirculation region, followed by a progressive recover up to the next shedding. However, neither the experiment nor the LES has captured any specific frequency of the vortex shedding (the experimental spectra can be found in Ref. 50; for the LES, spectra will be introduced later in Section V B). Hence, the authors assume that the unsteady vortex shedding process is aperiodic. This may relate to the bimodal behavior observed previously in the experiment[26] and also in the LES results,[51] and further investigations are ongoing by the present authors.

B. One-point velocity spectral analysis

One-point velocity spectra as well as energy integral length scales can provide insights into how the turbulent kinetic energy (TKE) distributes, i.e., whether the TKE concentrates on large-scale eddies or on small scale eddies, and how the TKE develops when going across the corner separation region.

In order to realize these analyses, eight numerical probes have been put in the flow field to capture high resolution signals across the corner separation region (at $z/h = 1.4\%$). They are illustrated in Fig. 14 by red symbols. The first two points are upstream of the corner separation, the third point lies on the mean separation line, and the other points are within the corner separation.

The velocities obtained at these points are decomposed into three components: the tangential velocity component (u_s), the normal velocity component (u_n), and the spanwise velocity component (u_z). The definitions of u_s and u_n are shown in Fig. 10(c), and u_z points towards the mid-span.

In this paper, the normalization of the one-point velocity spectra follows the approach introduced by Metzger and Klewicki[52] and Perry and Abell.[53] The power spectral density ϕ_{uu} of the fluctuating velocity u' yields

$$\int_0^{+\infty} \phi_{uu}(f)df = \langle u'u' \rangle. \tag{10}$$

The following relationship is used to normalize the spectrum:

$$\int_0^{+\infty} \Phi_{uu}(\omega^+)d\omega^+ = \frac{\langle u'u' \rangle}{u_\tau^2}, \tag{11}$$

where ω^+ is given by

$$\omega^+ = \frac{2\pi\nu f}{u_\tau^2}, \tag{12}$$

and the normalized energy-spectrum is expressed by

$$\Phi_{uu}(\omega^+) = \frac{\phi_{uu}(f)}{2\pi\nu}. \tag{13}$$

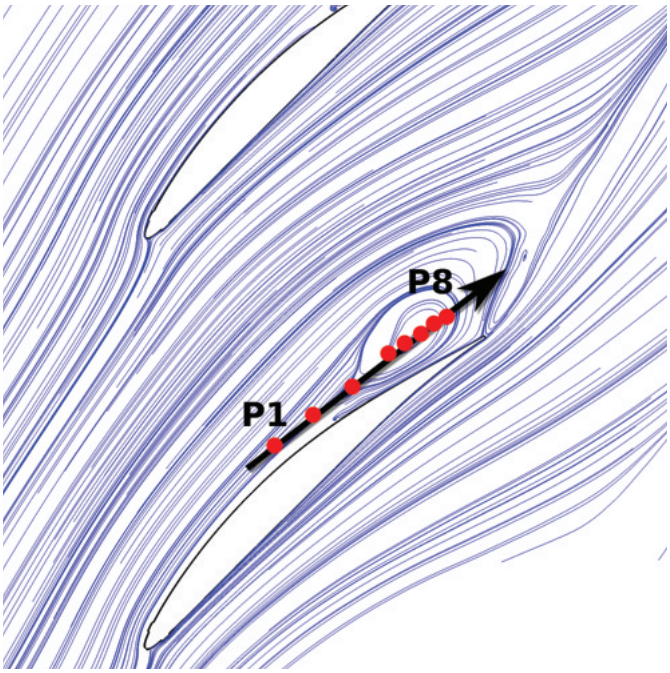

FIG. 14. Numerical probes through the corner separation region ($z/h = 1.4\%$).

The evolution of the one-point velocity spectra (tangential, normal, and spanwise components) is plotted in Fig. 15. For clarity, the results are staggered with one decade between each other, from bottom to top. Inspecting the tangential velocity spectra, the $-5/3$ slope range is larger for the points upstream of the corner separation region. Going across the corner separation region, the low frequency part of the velocity spectrum increases. This indicates an increase of the energy of the largest eddies. Also, upstream of the corner separation region, the spectrum drops two decades within the plotted range of frequencies. Within the corner separation, it drops six decades. This suggests that the turbulent energy concentrates on the large-scale eddies. The same observation is made from the normal and spanwise velocity spectra in the same figure.

Next, the evolution of the energy integral length scales along the numerical probes is analyzed. The energy integral length scale l is defined by the following equation:[54]

$$l = \frac{\int \frac{\Phi_{uu}(\omega^+)}{\omega^+} d\omega^+}{\int \Phi_{uu}(\omega^+) d\omega^+} \tag{14}$$

for a given velocity component u.

The energy integral length scales along the numerical probes are plotted in Fig. 16, for the three components of velocity. The length scales are relatively lower upstream of the corner separation, and they increase significantly on the corner separation border. This is consistent with the observation from Fig. 15. Energetic large-scale eddies develop within the separation region. This may be consistent with the observation of Laval *et al.*[47] that in a separation region, the near-wall longitudinal streaks of the boundary layer separate and contribute to the increase in the turbulent intensity at large scales.

C. Turbulent anisotropy

The merge of the suction side and the endwall boundary layers and the occurrence of the corner separation make the flow state quite complex, which should result in an unusual level of anisotropy within this area. The level of anisotropy can be measured by an analytical model of Lumley and Newman.[55]

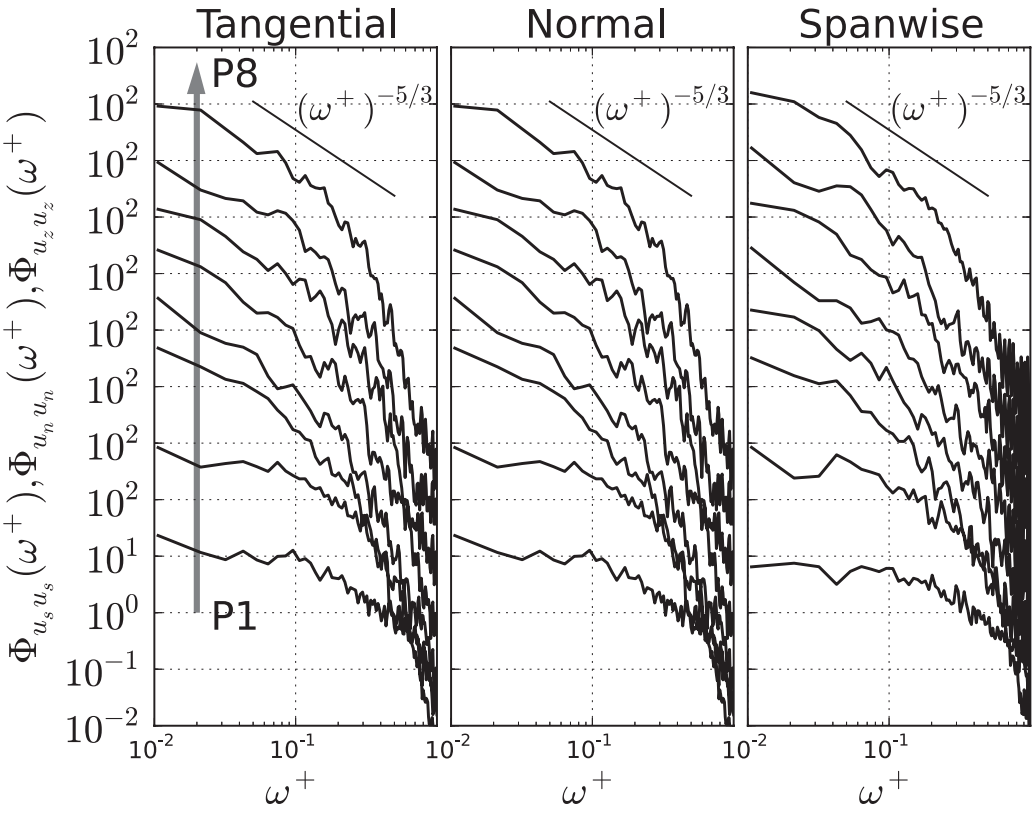

FIG. 15. Non-dimensional one-point velocity spectra.

According to Lumley and Newman,[55] an anisotropy tensor and two invariants are expressed as

$$b_{ij} = \frac{\langle u_i u_j \rangle}{\langle u_s u_s \rangle} - \frac{1}{3}\delta_{ij}, \tag{15}$$

$$II = b_{ij} b_{ji}, \tag{16}$$

$$III = b_{ij} b_{jk} b_{ki}. \tag{17}$$

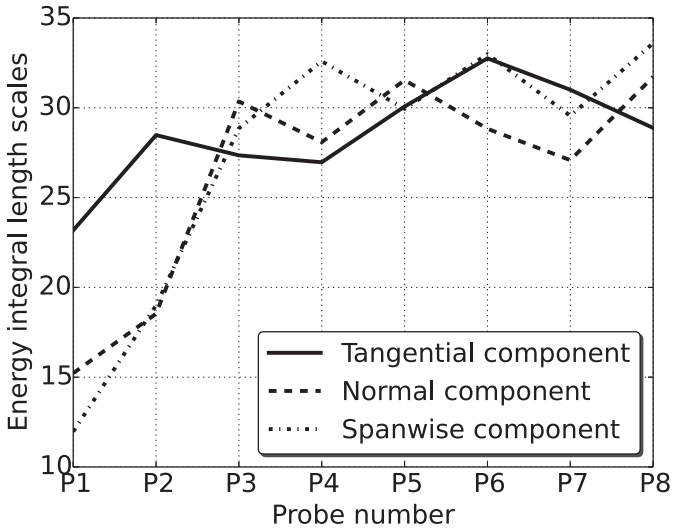

FIG. 16. Energy integral length scales (l).

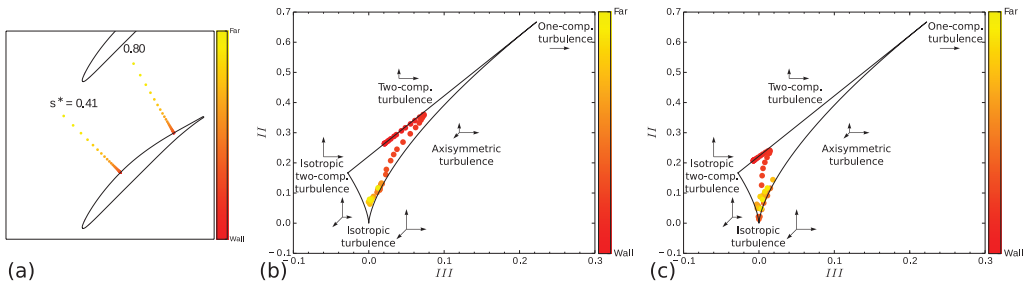

FIG. 17. Turbulent anisotropy maps near the end-plate ($z/h = 1.4\%$). (a) Measurement stations, (b) upstream of the corner separation ($s^* = 0.41$), and (c) within the corner separation ($s^* = 0.80$).

Figure 17(a) shows the two measurement stations selected for the analysis close to the end-wall ($z/h = 1.4\%$). One is upstream of the corner separation ($s^* = 0.41$) and the other one is within the corner separation region ($s^* = 0.80$). The distance from the wall is denoted by the color. The corresponding turbulent anisotropy maps are plotted in Figs. 17(b) and 17(c).

The Lumley triangle is defined by

$$II = \frac{3}{2}\left(\frac{4}{3}|III|\right)^{2/3}, \tag{18}$$

$$II = \frac{2}{9} + 2III. \tag{19}$$

It is plotted in Figs. 17(b) and 17(c), and all the realizable turbulent states should be enclosed in this triangle. The left and right curved boundaries correspond to axisymmetric turbulence. On the left curve, the axial component of fluctuations is smaller than the other two, and on the right curve, it is larger. The upper boundary corresponds to two-component turbulence. The bottom vertex represents isotropic turbulence. Along the left curve, one component degrades gradually, leading to isotropic two-component turbulence on the left vertex. Along the right curve, two components of turbulence decrease in the same time and finally leave one-component turbulence at the right vertex. Along the diagonal straight line from left to right, one component of initially isotropic two-component turbulence vanishes until the right summit, leaving one-component turbulence.

According to the LES, on the first measurement station (Fig. 17(b)), the flow state begins as two-component turbulence very close to the blade surface. Then, it moves toward the one-component turbulence, which corresponds to the first peak of the velocity fluctuations near the wall, as shown in Fig. 11(d). After reaching the peak toward one-component turbulence, the flow state drops toward isotropic turbulence. Within the corner separation region (Fig. 17(c)), the flow state goes quite differently. The near-wall peak toward one-component turbulence is less pronounced. Then, the flow state drops rapidly toward isotropic turbulence. This suggests that the flow state is "more isotropic" within the corner separation region. This is consistent with the close values of the integral length scales observed for the three components of velocity in Fig. 16.

VI. CONCLUSIONS

The objective of the present study was to investigate the characteristics of the corner separation encountered in a linear compressor cascade. The LMFA-NACA65 linear compressor cascade, with a chord-based Reynolds number $Re_c = 3.82 \times 10^5$, has been designed and investigated experimentally in a previous work. A detailed and accurate experimental database about corner separation has been built up. In the present work, a wall-resolved LES of this configuration has been carried out and analyzed.

The boundary conditions, especially the inflow condition, are treated and validated very carefully in comparison with the experimental results. The subgrid-activity of the simulation proves to be satisfactory.

The fidelity of the LES results is assessed with experimental results. The corner separation at the junction between the end-wall (hub) and the blade suction surface is captured by both the experiment and the LES. The LES appears to accurately predict the corner separation in terms of (i) the blade static pressure coefficient, (ii) the total pressure loss coefficient, (iii) the mean velocity profiles, and (iv) the velocity fluctuations along the blade suction surface.

By inspecting the evolution of the turbulent structures, it is found that the unsteadiness of the separation envelope may relate to an aperiodic vortex shedding process. Neither the experiment nor the LES has captured a specific frequency. According to the one-point velocity spectral analysis, through the corner separation region, the large-scale energy increases and the turbulent energy concentrates on the largest eddies. The energy integral length scales appear to increase for the three components of velocity. The turbulent anisotropy analysis suggests that the flow state changes significantly from the region upstream of the corner separation to the region within the corner separation and exhibits more isotropic characteristics.

Some work should continue: (i) the relationship between the aperiodic vortex shedding and the bi-modal phenomenon observed in both the experiment and the LES should be further studied; (ii) the turbulent kinetic energy budget that can be obtained from the LES should be analyzed to interpret the turbulent transport nature within the corner separation; (iii) with better understandings of the corner separation mechanisms, an investigation on control of the corner separation should be conducted.

ACKNOWLEDGMENTS

Feng Gao would like to thank Joëlle Caro for her efficient technical support. The present work was supported by the Franco-Chinese project AXIOOM, funded by the French National Research Agency (ANR) and the National Natural Science Foundation of China (NSFC). The authors also wish to express their sincere gratitude to the support from the NSFC (No. 51420105008). This work was performed using the HPC resources from GENCI-CINES (Grant No. 2014-2a6081).

[1] D. Wisler, "Loss reduction in axial-flow compressors through low-speed model testing," J. Eng. Gas Turbines Power **107**, 354–363 (1985).
[2] B. Lakshminarayana, *Fluid Dynamics and Heat Transfer of Turbomachinery* (Wiley-Interscience Publication, 1996).
[3] Y. Dong, S. J. Gallimore, and H. P. Hodson, "Three-dimensional flows and loss reduction in axial compressors," J. Turbomachinery **109**(3), 354–361 (1987).
[4] H. D. Schulz, H. E. Gallus, and B. Lakshminarayana, "Three-dimensional separated flow field in the endwall region of an annular compressor cascade in the presence of rotor-stator interaction: Part 1—Quasi-Steady flow field and comparison with steady-state data," J. Turbomachinery **112**, 669–678 (1990).
[5] A. M. Yocum and W. F. O'Brien, "Separated flow in a low-speed two-dimensional cascade: Part I—Flow visualization and time-mean velocity measurements," J. Turbomachinery **115**, 409–420 (1993).
[6] C. Hah and J. Loellbach, "Development of hub corner stall and its influence on the performance of axial compressor blade rows," J. Turbomachinery **121**, 67–77 (1999).
[7] S. A. Gbadebo, N. A. Cumpsty, and T. P. Hynes, "Three-dimensional separations in axial compressors," J. Turbomachinery **127**, 331–339 (2005).
[8] V.-M. Lei, "A simple criterion for three-dimensional flow separation in axial compressors," Ph.D. thesis, Massachusetts Institute of Technology, 2006.
[9] M. Choi, J. H. Baek, S. H. Oh, and D. J. Ki, "Role of hub-corner-separation on rotating stall in an axial compressor," Trans. Jpn. Soc. Aeronaut. Space Sci. **51**, 93–100 (2008).
[10] E. Lewin, D. Kožulović, and U. Stark, "Experimental and numerical analysis of hub-corner stall in compressor cascades," in *Proceedings of ASME Turbo Expo 2010: Power for Land, Sea and Air*, *Glasgow, UK*, *June 14–18, 2010* (American Society of Mechanical Engineers), pp. GT2010-22704.
[11] W. Ma, "Experimental investigation of corner stall in a linear compressor cascade," Ph.D. thesis, École Centrale de Lyon, 2012.
[12] F. Gand, S. Deck, V. Brunet, and P. Sagaut, "Flow dynamics past a simplified wing body junction," Phys. Fluids **22**, 115111 (2010).
[13] F. Gao, "Advanced numerical simulation of corner separation in a linear compressor cascade," Ph.D. thesis, École Centrale de Lyon, 2014.
[14] X. Ottavy, S. Vilmin, M. Opoka, H. Hodson, and S. Gallimore, "The effects of wake-passing unsteadiness over a highly-loaded compressor-like flat plate," J. Turbomachinery **126**, 13–23 (2004).
[15] S. A. Gbadebo, N. A. Cumpsty, and T. P. Hynes, "Interaction of tip clearance flow and three-dimensional separations in axial compressors," J. Turbomachinery **129**, 679–685 (2007).
[16] S. C. Back, G. V. Hobson, S. J. Song, and K. T. Millsaps, "Effects of Reynolds number and surface roughness magnitude and location on compressor cascade performance," J. Turbomachinery **134**, 051013 (2012).

[17] A. Weber, H.-A. Schreiber, R. Fuchs, and W. Steinert, "3-d transonic flow in a compressor cascade with shock-induced corner stall," J. Turbomachinery **124**, 358 (2002).
[18] M. N. Goodhand and R. J. Miller, "The impact of real geometries on three-dimensional separations in compressors," J. Turbomachinery **134**, 021007 (2012).
[19] A. Marsan, I. Trébinjac, S. Coste, and G. Leroy, "Study and control of a radial vaned diffuser stall," Int. J. Rotating Mach. **2012**, 1–12.
[20] K. K. George, S. N. A. Sunkara, J. T. George, M. Joseph, A. M. Pradeep, and B. Roy, *Investigations on Stator Hub End Losses and its Control in an Axial Flow Compressor* (American Society of Mechanical Engineers, 2014), p. V02AT37A047.
[21] K. Liesner and R. Meyer, *Combination of Active and Passive Flow Control in a High Speed Compressor Cascade* (American Society of Mechanical Engineers, 2014), p. V02AT37A017.
[22] M. G. D. Giorgi, E. Pescini, F. Marra, and A. Ficarella, *Experimental and Numerical Analysis of a Micro Plasma Actuator for Active Flow Control in Turbomachinery* (American Society of Mechanical Engineers, 2014), p. V02AT37A011.
[23] D. Wang, W. Ma, and L. Lu, "Modification of SA turbulence model on separation flows," J. Propul. Technol. **5**, 006 (2008).
[24] Y. Liu, L. Lu, L. Fang, and F. Gao, "Modification of Spalart-Allmaras model with consideration of turbulence energy backscatter using velocity helicity," Phys. Lett. A **375**, 2377–2381 (2011).
[25] F. Gao, W. Ma, J. Boudet, X. Ottavy, L. Lu, and F. Leboeuf, "Numerical analysis of three-dimensional corner separation in a linear compressor cascade," in *Proceedings of ASME Turbo Expo 2013: Turbine Technical Conference and Exposition* (American Society of Mechanical Engineers, San Antonio, Texas, USA, 2013), pp. GT2013-95581.
[26] W. Ma, X. Ottavy, L. Lu, and F. Leboeuf, "Intermittent corner separation in a linear compressor cascade," Exp. Fluids **54**, 1–17 (2013).
[27] W. Ma, X. Ottavy, L.-P. Lu, and F. Leboeuf, "Effect of an adverse pressure gradient on the streamwise Reynolds stress profile maxima in a turbulent boundary layer," Acta Mech. Sin. **29**, 395–398 (2013).
[28] D. You, R. Mittal, M. Wang, and P. Moin, "Computational methodology for large-eddy simulation of tip-clearance flows," AIAA J. **42**, 271–279 (2004).
[29] J. Boudet, J. Caro, L. Shao, and E. Lévêque, "Numerical studies towards practical large-eddy simulation," J. Therm. Sci. **16**, 328–336 (2007).
[30] F. Gand, "Dynamique des écoulements de jonction en régime turbulent," Ph.D. thesis, Université Pierre et Marie Curie, 2011.
[31] J. Boudet, A. Cahuzac, P. Kausche, and M. C. Jacob, "Zonal large-eddy simulation of a fan tip-clearance flow, with evidence of vortex wandering," J. Turbomachinery **137**, 061001 (2015).
[32] W. Ma, X. Ottavy, F. Lu, L. Leboeuf, and F. Gao, "Experimental study of corner stall in a linear compressor cascade," Chin. J. Aeronaut. **24**, 235–242 (2011).
[33] B. J. Evans, "Effects of free-stream turbulence on blade performance in a compressor cascade," Ph.D. thesis, University of Cambridge, 1971.
[34] L. Smati, S. Aubert, P. Ferrand, and F. Massao, "Comparison of numerical schemes to investigate blade flutter," in *Unsteady Aerodynamics and Aeroelasticity of Turbomachines*, edited by T. H. Fransson (Kluwer Academic Publishers, Stockholm, 1998), pp. 749–763.
[35] E. Lévêque, F. Toschi, L. Shao, and J.-P. Bertoglio, "Shear-improved Smagorinsky model for large-eddy simulation of wall-bounded turbulent flows," J. Fluid Mech. **570**, 491–502 (2007).
[36] A. Cahuzac, J. Boudet, P. Borgnat, and E. Lévêque, "Smoothing algorithms for mean-flow extraction in large-eddy simulation of complex turbulent flows," Phys. Fluids **22**, 125104 (2010).
[37] L. Shao, S. Sarkar, and C. Pantano, "On the relationship between the mean flow and subgrid stresses in large eddy simulation of turbulent shear flows," Phys. Fluids **11**, 1229–1248 (1999).
[38] A. Jameson, W. Schmidt, E. Turkel *et al.*, "Numerical solutions of the Euler equations by finite volume methods using Runge-Kutta time-stepping schemes," AIAA paper No. 81-1259, 1981.
[39] J. Boudet, J.-F. Monier, and F. Gao, "Implementation of a roughness element to trip transition in large-eddy simulation," J. Therm. Sci. **24**, 30–36 (2015).
[40] C. Bogey and C. Bailly, "Three-dimensional non-reflective boundary conditions for acoustic simulations: Far field formulation and validation test cases," Acta Acust. Acust. **88**, 463–471 (2002).
[41] J. A. Sillero, J. Jiménez, and R. D. Moser, "One-point statistics for turbulent wall-bounded flows at Reynolds numbers up to $\delta^+ \approx 2000$," Phys. Fluids **25**, 105102 (2013).
[42] F. Bario, F. Leboeuf, and K. Papailiou, "Study of secondary flows in blade cascades of turbomachines," J. Eng. Gas Turbines Power **104**, 497–509 (1982).
[43] C. Beselt, M. Eck, and D. Peitsch, "Three-dimensional flow field in highly loaded compressor cascade," J. Turbomachinery **136**, 101007 (2014).
[44] J. Ye, "Large-eddy simulation of blade boundary layer spatio-temporal evolution under unsteady disturbances," Ph.D. thesis, Beihang University, 2009.
[45] B. J. Geurts and J. Fröhlich, "A framework for predicting accuracy limitations in large-eddy simulation," Phys. Fluids **14**, L41–L44 (2002).
[46] V.-M. Lei, Z. Spakovszky, and E. Greitzer, "A criterion for axial compressor hub-corner stall," J. Turbomachinery **130**, 031006 (2008).
[47] J.-P. Laval, M. Marquillie, and U. Ehrenstein, "On the relation between kinetic energy production in adverse-pressure gradient wall turbulence and streak instability," J. Turbul. **13**, N21 (2012).
[48] J. C. Hunt, A. Wray, and P. Moin, "Eddies, streams, and convergence zones in turbulent flows," in *Studying Turbulence Using Numerical Simulation Databases, 2* (Stanford University, 1988), Vol. 1, pp. 193–208.
[49] L.-W. Chen, C.-Y. Xu, and X.-Y. Lu, "Numerical investigation of the compressible flow past an aerofoil," J. Fluid Mech. **643**, 97–126 (2010).

[50] G. Zambonini, "Assessment of microphone and 2.5D hot-wire measurements for the characterization of the unsteadiness of a corner separation," Master's thesis, École Centrale de Lyon, 2013.
[51] F. Gao, G. Zambonini, J. Boudet, X. Ottavy, L. Lu, and L. Shao, "Unsteady behavior of corner separation in a compressor cascade: Large eddy simulation and experimental study," Proc. Inst. Mech. Eng., Part A **229**(5), 508–519 (2015).
[52] M. M. Metzger and J. C. Klewicki, "A comparative study of near-wall turbulence in high and low Reynolds number boundary layers," Phys. Fluids **13**, 692–701 (2001).
[53] A. E. Perry and C. J. Abell, "Scaling laws for pipe-flow turbulence," J. Fluid Mech. **67**, 257–271 (1975).
[54] S. B. Pope, *Turbulent Flows* (Cambridge University Press, 2000).
[55] J. L. Lumley and G. R. Newman, "The return to isotropy of homogeneous turbulence," J. Fluid Mech. **82**, 161–178 (1977).